Article | Received 26 June 2026; Revised 13 August 2026; Accepted 16 August 2026; Published 27 August 2026
https://doi.org/10.55092/am20260011

Rotary ultrasonic machining of single-crystal silicon

Kh M Asif Raihan[1], Isaac Obembe[1], Deven Wieland[2], Christopher Jones[3] and Meng Zhang[1,*]

[1] Department of Industrial and Manufacturing Systems Engineering, Kansas State University, Manhattan, USA
[2] John Deere, Coffeyville, USA
[3] Department of Civil Engineering, Kansas State University, Manhattan, USA

* Correspondence author; E-mail: meng@ksu.edu.

Highlights:

- Hole-making in single-crystal silicon with RUM.
- Microscopy and nanoindentation revealed a hybrid ductile-brittle removal mechanism.
- Ultrasonic vibration-assistance reduced silicon cutting force by up to 29%.
- Improved hole quality with low feedrate, high spindle speed and high ultrasonic power.
- Minimal tool wear and controlled edge chipping during RUM.

Abstract: Precision machining of single-crystal silicon components presents critical challenges for the semiconductor and photovoltaic industries due to its high hardness and low fracture toughness. Conventional machining processes are often susceptible to workpiece breakage and subsurface damage, along with high tool wear and poor surface finish. Recent studies have increasingly focused on achieving ductile mode machining of single-crystal silicon using nontraditional machining processes; yet studies on the material removal mechanism remain limited. In this study, the feasibility of rotary ultrasonic machining (RUM) of single-crystal silicon and the material removal mechanism were investigated. The material removal mechanism study via microscopic imaging, motion simulation, and nanoindentation experiments revealed that RUM promoted localized ductile deformation during silicon machining, resulting in a hybrid ductile-brittle material removal mode. The effects of input variables (feedrate, spindle speed, and ultrasonic power) on cutting force, surface roughness, geometrical accuracy of the machined holes, and edge chipping sizes were also evaluated. The results showed that ultrasonic vibration assistance effectively reduced cutting force, while hole quality improvement and edge chipping mitigation were achieved through appropriate selection of machining parameters. Compared with conventional machining conditions, tool wear was also minimal during RUM.

Keywords: brittle materials; cutting force; material removal; nanoindentation; silicon; surface roughness; ultrasonic machining

Copyright©2026 by the authors. Published by ELSP. This work is licensed under Creative Commons Attribution 4.0 International License, which permits unrestricted use, distribution, and reproduction in any medium provided the original work is properly cited.

1. Introduction

Single-crystal (monocrystalline) silicon is the cornerstone material in microelectronics and optoelectronics, which often requires ultra-precise dimensions and surface integrity to meet the stringent requirements of semiconductor and photovoltaic applications [1–4]. In semiconductor manufacturing, gas distribution plates, electrostatic wafer chucks, and other silicon-based components require intricate networks of micro-holes and channels with high dimensional tolerances and surface quality specifications [5–7]. In photovoltaic manufacturing, monocrystalline silicon ingots need to be sliced into ultra-thin wafers (180–240 microns thick), and the cutting process directly impacts solar cell efficiency [8]. However, silicon having a highly ordered and stable diamond cubic crystal lattice structure along with a moderate bandgap, features strong covalent bonds that resist plastic deformation, resulting in predominantly brittle fracture under cutting stress [9,10]. Silicon's brittleness leads to issues such as subsurface damage, edge chipping, and surface cracking that can compromise component performance and contaminate semiconductor processing environments. Additionally, silicon's high hardness (approximately~12 GPa) may cause severe tool wear in conventional machining processes, while its low fracture toughness (0.70–1.00 MPa·m$^{\wedge 1/2}$) makes it prone to failure during material removal operations [11].

Recognizing the limitations of conventional machining, researchers have explored non-traditional machining approaches of multiple domains, such as mechanical (ultrasonic machining, water jet machining, abrasive jet machining), thermoelectric (plasma arc machining, laser beam machining, electric discharge machining), and chemical (chemical etching, electrochemical machining) methods for silicon processing [12,13]. Table 1 summarizes these methods investigated for hole-making in single-crystal silicon. Firstly, Smith *et al.* [14] machined holes using a high-speed spindle (90,000–100,000 rpm) on a lathe setup with diamond abrasives deposited on steel and tungsten carbide mandrels. A radial increment of 12.70 μm per pass was used, but significant microcracks and tool wear were reported. Luft *et al.* [15] employed nanosecond pulsed copper vapor lasers (15 J/cm²) to mitigate material breakage, though redeposition and cracks up to 8 μm from the hole wall were observed. UV nanosecond lasers [16,17] achieved 20–30 μm diameter holes for interconnects and LEDs, while femtosecond and picosecond lasers [18,19] faced challenges in thermal load management. Maclean *et al.* [20] used a CW Yb fiber laser, showing shorter cracks but some ellipticity at higher power. Unoa *et al.* [21] applied EDM with copper plates to drill single-crystal silicon, though copper contamination and oxide buildup were concerns. Mohammadi and Patten [22] demonstrated laser-augmented diamond drilling, where thermal softening improved ductile-to-brittle transition depth and material removal rate, but high laser power risked surface burning and non-uniform hole geometry. Micro-ultrasonic drilling of single-crystal silicon using silicon carbide slurry was also reported, where an optimization model was employed to determine the machining parameters [23]. Commercial machine systems like Micro PCD drills (TELCON diamond ltd. PCD cutting tools, Afula, Israel) and Ultrasonic 55 micro drill (DMG MORI, USA, Hoffman Estates, Illinois) have also been used for silicon drilling.

Table 1. Methods for drilling holes in single-crystal silicon.

Methods	Principles	Process parameters	Hole dimension	References
Diamond drilling	Nickel bonded Diamond cutters with 40–100 µm grit size attached with high-speed spindles	Spindle speed: 90,000–100,000 rpm Feedrate: 12.70 µm/pass	Depth: 15 mm Diameter: 12 mm	[14]
Nanosecond laser drilling	Melting and vaporization by absorption of nanosecond pulsed laser	Pulse duration: 40 ns–810 ns Wavelength: 250 nm–350 nm Beam diameter: 15–25 µm	Depth: 120 µm Diameter: 25 µm	[15–17]
Millisecond laser drilling	Melting and vaporization by absorption of millisecond pulsed laser	Pulse duration: 2 ms Power:1.4 kW Wavelength: 1070 nm Beam diameter: 400 µm	Depth: 500 µm Diameter: 550 µm	[20]
Electric discharge machining	Melting of silicon by spark erosion from an electrode	Discharge current: 2–15A Pulse duration: 4–28 µs Removal rate: 0.05–0.50 mm/s	Depth: 5 mm Diameter: 1 mm	[21]
Laser assisted diamond drilling	Material softening with laser beam and material removal with a diamond cutting tool	Laser type: IR CW fiber Max power: 100 W Drill bit radius: 0.50 mm Spindle speed: 1000 rpm Feedrate: 2 µm/s	Depth: 40–80 µm Diamete: 500 µm	[22]
Ultrasonic machining	Impacting and grinding with abrasive slurry	Spindle speed: 200–400 rpm Ultrasonic power: 30%–50% Abrasive flow: 15 L/min	Depth: 1 mm Diameter: 600 µm	[23]

Despite these advances, critical knowledge gaps remain in both process capability and comprehensive understanding of the material behavior during single-crystal silicon machining. Specifically, existing silicon hole making studies lack comprehensive analysis of the underlying material removal mechanisms and their correlation with machining parameters for attaining superior surface integrity.

In recent years, ultrasonic vibration-assisted machining has been explored for efficient machining of brittle materials. It enables intermittent contact between the cutting tool and the workpiece [24]. The intermittent contact can facilitate material separation through localized stress concentration and cyclic loading-unloading, which promotes micro-crack initiation and crack growth suppression. Building on this principle, rotary ultrasonic machining (RUM) integrates ultrasonic vibration with conventional core drilling using diamond abrasives to further enhance machining performance for brittle materials [25]. RUM uses a rotating diamond-impregnated tool with high-frequency (≥ 20 kHz) vibration. Table 2 summarizes key experimental and computational studies published in recent years (2021–2026) on ultrasonic vibration-assisted machining of brittle materials, and their findings.

Table 2. Recent ultrasonic machining studies for brittle materials and key findings (2021–2026).

Process	Materials	Key findings	Reference
Ultrasonic machining using abrasive slurry (USM)	Soda-lime glass	Material removal model for a single abrasive was developed. Abrasive impact velocity, USM power and tool-workpiece gap were most significant for effective machining	[26]
	Zirconia	Material removal was analyzed on the basis of machining marks. Effects of abrasive concentration and abrasive size on MRR were discussed.	[27,28]
	Monocrystalline silicon	Brittle-plastic transition kinetic energy model was developed to analyze the effect of process parameters on surface quality	[29]
	Inconel 718	Material removal behavior though nanoscratch test, nanoindenter and tool wear model was analyzed. Effect of process parameters on MRR and tool wear was studied.	[30,31]
Ultrasonic vibration assisted grinding (UVAG)	Composites-SiCp/Al, C/SiC, CFRP, SiC_f/SiC, Ti matrix composite	Influence of the composite anisotropy on material removal behavior was analyzed. Promotion of plastic deformation, transition of plastic deformation to brittle fracture, brittle-plastic synergistic removal and influence of the input parameters on cutting force and surface roughness were studied	[32–36]
	Ceramics- SiC, SiN, Alumina, Zirconia	Material removal mechanism and ductile removal to brittle fracture transition with undeformed chip thickness, scratch test, simulation model, crack inhibiting effect and effect of the input parameters were studied.	[37–40]
	Alloys- Inconel 718, Ni single crystal alloy, γ-TiAl alloy, Ti-6Al-4 V alloy, iron alloy	Motion path analysis, FEM and MD simulation, plastic deformation and chip formation were analyzed. Effect of ultrasonic vibration on grinding force, grinding temperature and surface morphology were studied	[41–45]
	Sapphire	Directional ultrasonic vibration study on the anisotropic crystal structure was done. Subsurface damage and surface roughness model was developed to study the material removal behavior	[46,47]
	Glass- borosilicate glass, monocrystalline glass	Influence of the ultrasonic assistance on the critical undeformed thickness for plastic removal was studied with cutting energy model and motion trajectory analysis.	[48,49]
Ultrasonic vibration assisted milling (UVAM)	Alloys-Ti-6Al-4V, TC18, Inconel 718, GH4169D superalloy, Al-50 wt % Si alloy, Ti2AlNb intermetallic alloy	Material removal mechanism was investigated with tool path trajectory, amplitude variation, and chip morphology studies. Milling under dry condition, formation of ultrasonic vibration texture and surface roughness of the machined surface was analyzed.	[50–54]

Table 2. *Cont.*

Process	Materials	Key findings	Reference
	Composites- SiC_p/Al, C_f/SiC, CFRTP, C/C, SiC_f/Al	Interaction between the constituent phase and ultrasonic vibration, single-fiber cutting simulation, effect of the vibration amplitude on removal mechanism and surface morphology were studied.	[55–59]
Ultrasonic vibration assisted polishing (UVAP)	Optical glass (K9, BK7), S136 steel, SiC	Material removal and polishing force models for UVAP were developed considering tool geometry, tilt and pressure distribution. Alternatively, self-excited vibration-assisted polishing with eccentric flexible ball-end tool was also reported along with material removal model and improved MRR.	[60–63]
Rotary ultrasonic machining	Ceramics- Zirconia, glass ceramic	Material removal mechanism was investigated through single abrasive analysis, cutting model with brittle fracture, and grinding mark analysis. Cutting force and surface roughness reduction were studied.	[64–66]
	Composites- CFRP, SiC_f/SiC, SiO2f/SiO2	Motion path of a single abrasive, scratch test, and fracture analysis were done to investigate the material removal mechanism and to analyze the effect of composite anisotropy. Effects of spindle speed, feedrate and ultrasonic amplitude on cutting force and surface roughness were studied.	[67–70]

These works signify the importance of studying the material removal behavior to understand the effects of machining parameters on surface roughness, subsurface damage and material removal rate. However, detailed investigation on the material removal mechanisms along with brittle-to-ductile transition (BDT) behavior, pressure-induced phase transformations, and crystallographic orientation effects during RUM of single-crystal silicon has received limited attention.

Here in this study, we focus on a comprehensive investigation of RUM of bulk monocrystalline silicon for hole-making operations. The research objectives are threefold: (1) elucidate material removal mechanism through nanoindentation experiments, motion simulation, and microscopy; (2) demonstrate the feasibility of RUM for single-crystal silicon machining; (3) establish relationships between process parameters (feedrate, spindle speed, ultrasonic power) and machining outcomes such as cutting forces, surface quality, geometrical accuracy and tool wear.

A two-level, three-factor full factorial design of experiments (DOE) was employed with feedrate, spindle speed, and ultrasonic power selected as the input variables. Cutting force under different machining conditions was measured between 81.57 N to 57.56 N, demonstrating the effectiveness of RUM in reducing the cutting force. The machined holes were examined for the surface finish quality, and the average roughness value (R_a) was between 2–3 μm for all experiments. Geometrical accuracy of the machined holes was evaluated through roundness error, taper angle, and core diameter variability, and compared against conventional machining conditions. The feedrate was then increased up to four times than the DOE high level feedrate to further illustrate the effectivity of ultrasonic power under high feedrate condition. Edge chipping size at the exit of the holes were measured and correlated with machining parameters. Cutting tool wear was studied by comparing different wear modes from micrographs of the cutting tool before and after machining.

2. Methods

2.1. Theoretical basis

2.1.1. Kinematic analysis of RUM

Figure 1 depicts the RUM cutting tool and workpiece interaction. The motion of individual diamond abrasives embedded on the RUM tool surface follows a complex three-dimensional helical trajectory that combines rotational motion with superimposed ultrasonic oscillation. The trajectory of single diamond abrasive can be described by Equation (1) [32]:

$$\begin{cases} X(t) = R\sin\omega t \\ Y(t) = R\cos(\omega t) \\ Z(t) = A\sin(2\pi f t) + v_w t \end{cases} \quad (1)$$

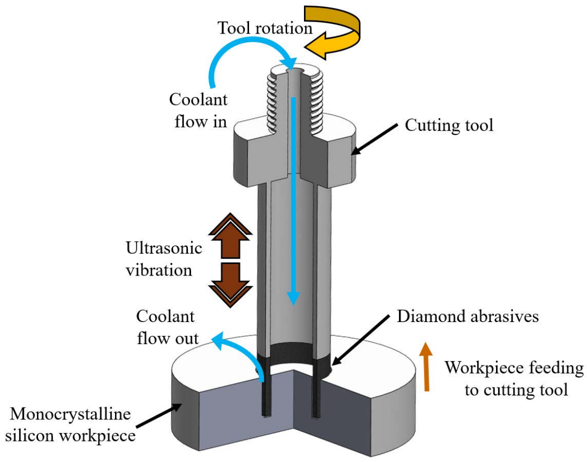

Figure 1. Illustration of RUM.

where R represents the tool radius, ω is the angular velocity, A is the ultrasonic amplitude, f is the ultrasonic frequency, and v_w is the feedrate. Figure 2a depicts the motion of a single diamond abrasive in 3D space simulated based on Equation (1), which demonstrates how a single particle would travel vertically while cutting through the workpiece. Figure 2b demonstrates the motion in 2D space, which shows the characteristic sinusoidal cutting pattern that directly influences surface morphology and material removal characteristics.

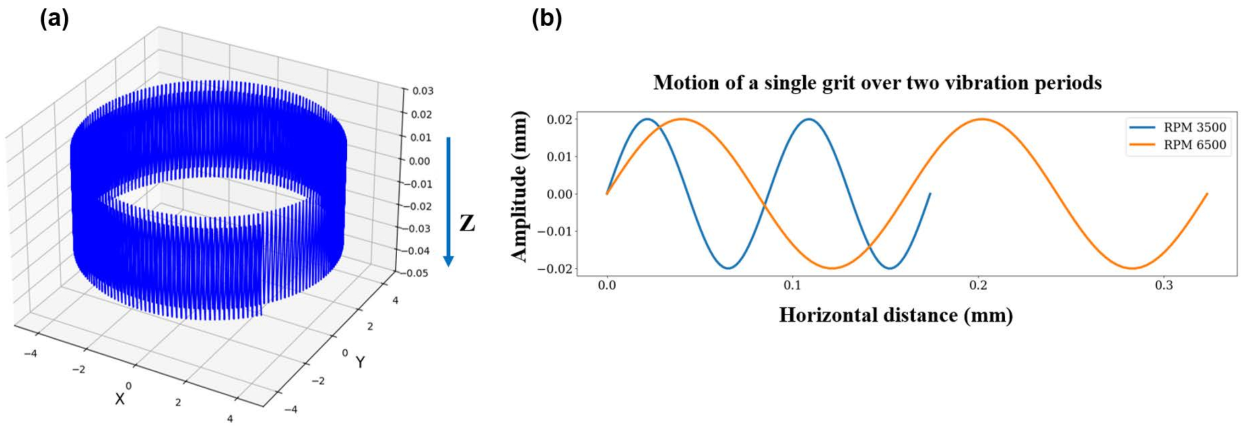

Figure 2. Motion of a single abrasive. **(a)** 3D space; **(b)** 2D motion at different spindle speeds.

Due to this sinusoidal motion, ultrasonic oscillation creates an intermittent contact between the diamond abrasives and the silicon workpiece with cycling loading-unloading phase. Material engagement or loading occurs only during the lower half-cycle when the tool moves toward the workpiece. The effective contact time represents approximately 30%–40% of each ultrasonic cycle, creating dynamic contact pressures that significantly exceed static loading conditions [65].

2.1.2. Crack formation and suppression in single-crystal silicon

Single-crystal silicon's diamond cubic crystal structure exhibits anisotropic mechanical properties due to its highly directional covalent sp^3 bonding [11]. Specifically, the surface energy and fracture toughness values are highly dependent on the crystallographic orientation. Table 3 shows the values in different plane direction.

Table 3. Surface energy and fracture toughness of single-crystal silicon [11].

Plane direction	Surface energy (J/m²)	Fracture toughness (MPa·√m)
{100}	2.40–2.84	0.95–1.05
{110}	1.30–1.44	0.90–1.00
{111}	1.15–1.24	0.70–0.80

As shown in Table 3, {111} plane has the least surface energy and fracture toughness values, and single-crystal silicon preferentially fractures along these planes under mechanical loading. The {110} planes exhibit slightly higher surface energy and fracture toughness, serving as secondary failure paths. In contrast, the {100} planes are the least favorable for crack propagation. Typically, for brittle materials, two principal crack systems can develop under abrasive particle contact loading, such as indentation—(1) radial cracks and (2) lateral cracks [71]. Figure 3 depicts the cracks formation under indentation with single diamond abrasive.

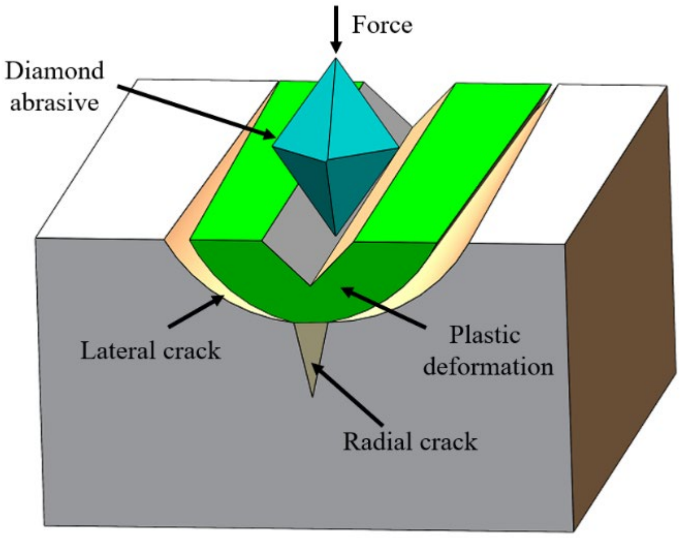

Figure 3. Principal cracks in brittle failures.

Firstly, radial (median) cracks initiate beneath the contact zone, governed by the Mohr-Coulomb criterion for brittle materials, which states failure occurs when the combination of shear stress and normal stress on a plane exceeds the material's critical threshold- $\tau = C_0 + \sigma_n \tan\varphi$, where τ represents the shear stress, σ_n is the normal stress, C_0 is the bond strength (material constant) and φ is the internal friction angle [72]. Once initiated, cracks propagate preferentially along {111} or {110} crystallographic planes, which represent energetically favorable cleavage as discussed before.

Secondly, lateral cracks nucleate parallel to the contact surface at depths of approximately 0.1–0.3 times the contact radius during unloading phases [73]. These cracks form due to the release of residual compressive stresses combined with tensile stress concentrations developed during the loading phase of the sinusoidal motion.

Furthermore, the classical Griffith criterion for crack propagation establishes that crack extension occurs when the energy release rate, G equals or exceeds the critical energy release rate $G_c = 2\gamma_s$, where 'γ_s' represents the surface energy [74]. For silicon, the critical energy release rates are approximately 2.3–2.9 J/m² for {111} cleavage and 2.6–2.9 J/m² for {110} cleavage [75].

The intermittent contact conditions generated by RUM can modify the local stress field and influence the initiation and propagation of both radial and lateral cracks. From the Mohr-Coulomb perspective, cyclic loading-unloading can locally reduce the duration of critical stress conditions, while from the Griffith perspective, intermittent contact may limit the energy available for crack growth. Therefore, localized crack suppression can occur along the {111} and {110} cleavage planes, however brittle fracture is still expected when local penetration depths or contact stresses exceed critical values.

2.1.3. Pressure induced phase transformation

Apart from the radial and lateral fractures, silicon undergoes a complex series of pressure-induced phase transformations that can fundamentally alter its mechanical behavior under high-pressure contact conditions. The primary transformation involves the conversion from Si-I (diamond cubic structure) to Si-II (β-tin structure) at critical pressures of approximately 11–13 GPa during loading [76,77]. This transformation is accompanied by a significant volume reduction of approximately 22% and a structural change from 4-fold tetrahedral coordination to 6-fold coordination, resulting in metallic behavior and substantially increased ductility compared to the original diamond cubic phase. During unloading, the high-pressure Si-II phase undergoes further transformations depending on the unloading rate and local stress state. Fast unloading typically results in the formation of amorphous silicon (a-Si), while slower unloading can produce metastable crystalline phases, such as Si-III (BC8 structure) or Si-XII (R8 structure). Due to the smaller edge radius of the diamond abrasives on RUM cutting tool and high impact loading, the local stress concertation can be high enough to achieve these residual transformed phases, which can create ductile zones that exhibit different mechanical properties compared to the original silicon crystalline structure, particularly enhanced resistance to crack propagation and improved plastic deformation capability. The maximum pressure calculation considering Hertzian contact has been provided in supplementary information section.

2.1.4. Critical cutting depth and intermittent contact in RUM

Bifano-Dow-Scattergood criterion describes the transition from brittle to ductile material removal for ductile regime machining of brittle materials [78]. The criterion relates the critical depth of cut to material properties through the relationship described by Equation (2).

$$d_c = \beta\left(\frac{K_c}{H}\right)^2\left(\frac{E}{H}\right) \quad (2)$$

where β represents a geometric constant for indenters, K_c is the fracture toughness, H is the hardness, and E is the elastic modulus of the workpiece material. For silicon with its typical material properties, the critical depth of cut ranges from approximately 50–150 nm depending on crystallographic orientation [79]. Operating with uncut chip thicknesses below this critical value promotes plastic flow mechanisms over brittle fracture, enabling the achievement of high-quality ductile surfaces.

With RUM, the instantaneous penetration depth during each engagement cycle is empirically determined to be approximately 10% of the ultrasonic amplitude [80]. As shown in Figure 4, maximum penetration occurs at the phase angle of $3\pi/2$ in the ultrasonic cycle, corresponding to maximum tool displacement toward the workpiece. Therefore, the intermittent vibration results in periodically varying penetration depths, which may influence the brittle-to-ductile transition behavior.

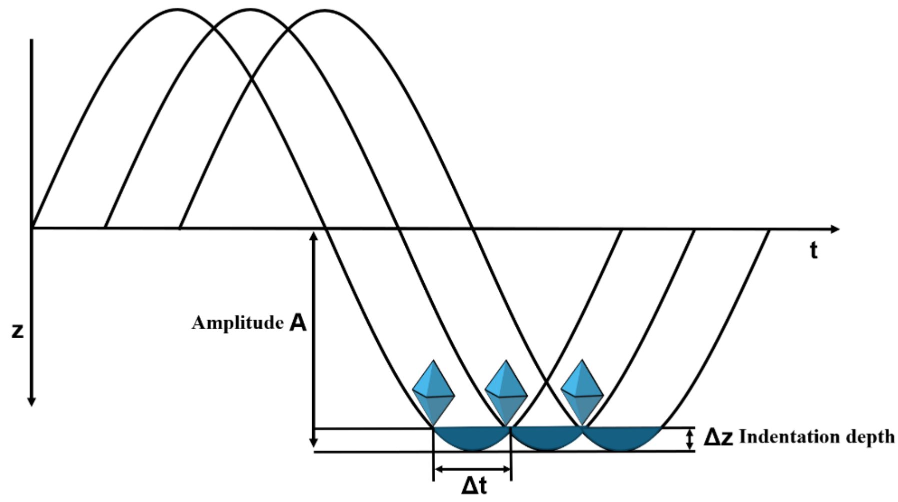

Figure 4. Indentation depth of single abrasive.

2.2. Materials

The workpiece was a single-crystal silicon disc with a diameter of 44.35 mm and a thickness of 8.44 mm. A core drill (NBR Diamond Tool Corp., NH) dressed with metal-bonded diamond abrasives at the cutting edge was employed. Its inside diameter was 9.76 mm and the outside diameter was 12.00 mm. A 7% water-based coolant (TRIM SOL, Master Fluid Solutions, Perrysburg, OH) was supplied through the center of the cutting tool at 500 mL/min to reduce the cutting temperature and remove machining debris.

2.3. Experimental conditions

Machining experiments were performed on a rotary ultrasonic machine (Series 10, Sonic-Mill Inc, Albuquerque, NM). The schematic diagram of the experimental setup is illustrated in Figure 5. The power supply converted low frequency (60 Hz) electricity to high frequency (20 KHz electrical energy. This energy was transformed into mechanical vibration through a piezoelectric converter located inside the ultrasonic spindle. The electric motor mounted above the ultrasonic spindle provided the rotational motion of the tool. An electric lifting stage was employed for vertical feeding of the workpiece towards the RUM tool, and the feedrate was controlled with a computer numerical control (CNC) motion control software.

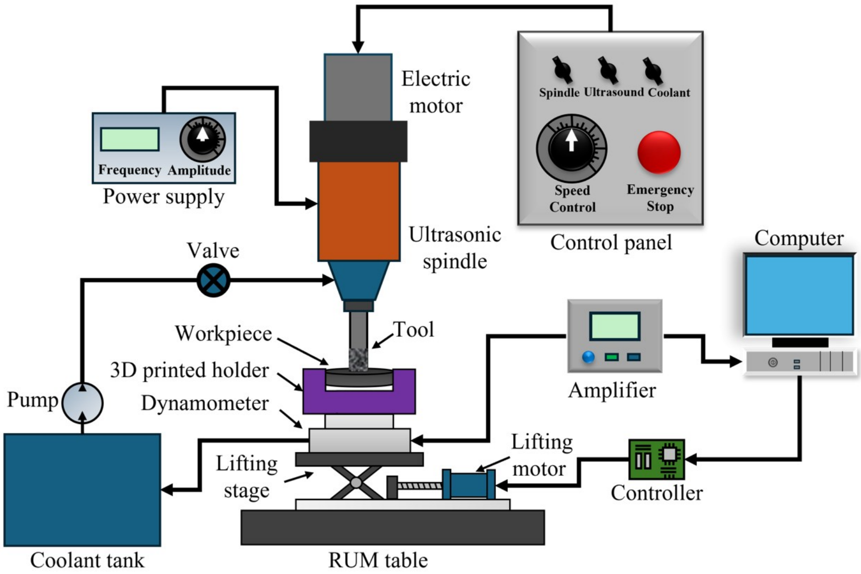

Figure 5. Rotary ultrasonic machining experimental set-up.

2.4. Nanoindentation

Nanoindentation experiments were carried out using a nano-indenter (Hysitron TI990, Bruker, Billerica, MA) to study the material removal mechanism. The nano-indenter was equipped with a Berkovich-type diamond indenter with sub-micron edge radius comparable to the abrasive particles coated on the RUM cutting tool. The maximum achievable peak load was 12 mN and the average stress applied was above 30 GPa, which exceeded the critical pressure required for pressure induced phase transformation of single-crystal silicon [81]. The instrument was also capable of superimposing a non-ultrasonic sinusoidal oscillation of up to 300 Hz on the static peak load, which was employed to qualitatively investigate the effects of cyclic loading-unloading on the deformation behavior. Furthermore, the nano-indenter was able to probe onto the sample surface to generate in-situ images of the sample before and after the indentation. The silicon samples were ground and polished with a series of abrasive papers and polishing pads before conducting nanoindentations. Experiments with two different test conditions were conducted: test (A)—indentation with a quasi-static 12 mN peak force and test (B) indentation with a 300 Hz sinusoidal oscillation superimposed with the 12 mN peak force.

2.5. Design of experiments

A two-level, three-factor (2^3) full factorial design was employed with 8 unique experimental conditions as listed in Table 4. The first input variable was feedrate which was controlled by the lifting stage. Secondly, ultrasonic power was reported as the power percentage level on the power supply unit. Finally, spindle speed was set on main control panel. A fully randomized run order was executed.

Table 4. Design of experiment.

Input variable	Unit	Low	High
Feedrate	$mm.min^{-1}$	10	30
Ultrasonic power	%	40	60
Spindle speed	rpm	3500	6500

2.6. Measurement procedures

2.6.1. Cutting force

The vertical cutting force was measured by a dynamometer (Kistler 9272, Kistler Instrument Corp, Switzerland) located underneath the workpiece holder. A charge amplifier (Kistler 5070, Kistler Instrument Corp, Switzerland) was used to amplify the signals from the dynamometer. Finally, the cutting force data was obtained from the DynoWare software (Version 2.6.5.16, Kistler Instrument Corp, Switzerland). A baseline correction would be performed if noticeable baseline drift happened during cutting force measurements due to the moisture sensitivity of the dynamometer with coolant. The maximum force value was used to represent the cutting force in all the measurements.

2.6.2. Surface roughness

RUM is a core drilling process that produces a hole and a rod after each machining experiment. To analyze the quality of the machined surface, surface roughness of the extracted rod was considered due to measurement convenience. A surface profilometer (SJ-400, Mitutoyo Corporation, Kanagawa, Japan) was used. The travel distance for each test was set as 4 mm, and both R_a and R_{max} values were recorded. Four different measurements were taken at every 90° rotation of the extracted rod. Finally, the average of the four values were reported as surface roughness results.

2.6.3. Edge chipping

The edge chipping width d_s was used to characterize the edge chipping size. As shown in Figure 6, d_s can be defined as $d_s = (D_m - D_h) / 2$ where D_m is the maximum diameter of the edge chipping profile, and D_h is the hole diameter. Hole-exit images were captured using a digital microscope (VHX-X1, Keyence Corp., Osaka, Japan), and D_m and D_h were determined by edge point identification and least-squares circle fitting in ImageJ (National Institutes of Health, Bethesda, MD, USA).

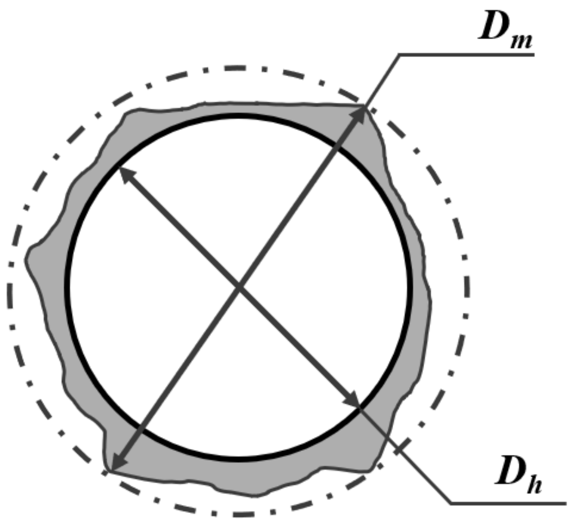

Figure 6. Definition of edge chipping size in this paper.

2.6.4. Geometrical accuracy

Hole geometrical accuracy was evaluated through roundness error, taper angle, and core diameter variability. Hole entrance and exit profiles, along with the extracted cores, were imaged using a digital microscope (VHX-X1, Keyence Corp., Osaka, Japan) and analyzed using ImageJ software (National Institutes of Health, Bethesda, MD, USA). Roundness error (R_e) was defined as $R_e = r_{max} - r_{min}$, where r_{max} and r_{min} are the maximum and minimum radial distances of the identified boundary points from the center of the fitted circle, respectively. Taper angle (θ) was determined from the entrance diameter and exit diameter as $\theta = \tan^{-1} [(D_{en} - D_{ex}) / (2t)]$, where D_{en} and D_{ex} are the entrance and exit hole diameters, respectively, and t is the thickness of the single-crystal silicon disc. Core diameter variability was characterized by the standard deviation of diameter measurements collected at 25 equally spaced locations along the extracted core in two orthogonal orientations.

2.6.5. Microscopy

To analyze the instantaneous surface morphology, the RUM cutting tool having different spindle speeds was briefly brought into contact with a polished silicon surface. The resulting imprints were examined using scanning electron microscopy (SEM) (Hitachi SU8230 FESEM, Tokyo, Japan). Additional microscopic images were also captured to investigate the morphology of the extracted rod after the hole-making process.

3. Results

3.1. Nanoindentation

Figures 7a depicts the depth profile of the indentation mark left on the single-crystal silicon sample from test A (indentation with a quasi-static 12 mN peak force). The maximum indentation depth was 63.77 nm without any radial crack propagation. Additionally, piled up silicon could be found up to a height of 26.77 nm at the edge of the indentation mark. Similar crack free indentations with material pile-ups were reported for nanoindentation experiments conducted in ductile materials like copper and aluminum, signifying that the material removal in test A was through ductile deformation [82].

The indentation depth profile from test B (indentation with a 300 Hz sinusoidal vibration superimposed with the 12 mN peak force) is provided in Figure 7b. A bigger indentation mark was observed with maximum indentation depth of 86.89 nm. The material pile-up at the edge of the mark also increased with the maximum pile height as 89.57 nm. No radial crack propagation was observed indicating the material removal was still through mainly plastic deformation. However, the increased indentation depth and increased pile-up height indicated that the hybrid motion of the indenter with vertical loading and oscillation could be influential for facilitating more significant plastic deformation. Furthermore, the absence fractures indicates that the applied pressure in the nanoindentation test potentially exceeded the threshold for pressure-induced phase transformation, thereby facilitating plastic deformation.

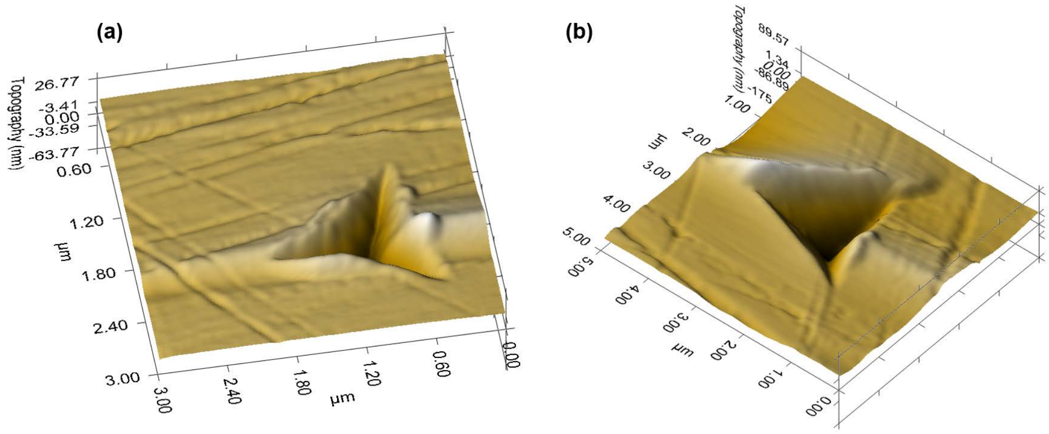

Figure 7. Depth profile of the indentation. **(a)** Without vibration; **(b)** with vibration.

3.2. Microscopy

Figure 8a,b shows the scanning electron microscopy images of the silicon top surfaces after scratching with the cutting tool. At the initial contact locations, significant material pile-ups can be noticed as shown in Figure 8a, whereas brittle fractures due to deeper penetrations are evident in Figure 8b. These findings further support the insights from nanoindentation experiments that the material pile-up at the edge of the indentation happens during the RUM process. At the same time, the coexistence of plastic deformation and brittle fracture suggests that the local stress concentration during RUM intermittently exceeded the critical pressure required for the Si-I → Si-II phase transformation. However, this criterion was not satisfied uniformly across all contact points, resulting in a mixed-mode material removal mechanism. To further explain this phenomenon, cutting force data from the experiments were used to estimate the maximum Hertzian contact pressure during RUM (detailed calculations are provided in supplemental information). Considering the measured cutting force range and diamond abrasive edge radii of 1–10 μm, the calculated maximum contact pressure ranged from 27.91 to 145.52 GPa (Supplementary Table S1). The pressure increased as the abrasive edge radius decreased. Since these values exceed the critical pressure required for the Si-I → Si-II phase transformation, localized phase transformation is expected to occur at some contact points. However, the actual contact pressure experienced by individual diamond abrasives can vary due to differences in abrasive geometry and instantaneous cutting force. Therefore, some contact regions may remain below the transformation threshold, contributing to the observed mixed-mode material removal mechanism.

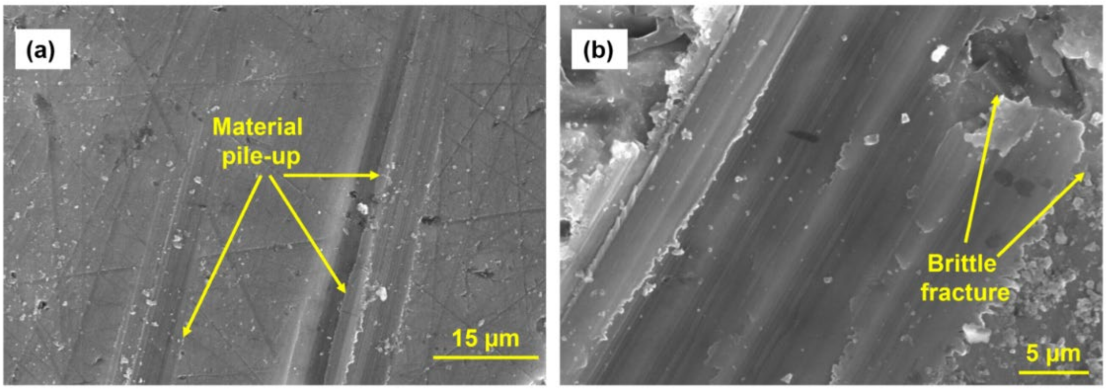

Figure 8. SEM images of the top surfaces after scratching with cutting tool. **(a)** Initial contact locations; **(b)** Brittle fractures with deeper penetrations.

Figures 9a,b show microscopic images of the extracted silicon rod. The images demonstrated abundance of sinusoidal machining streaks on the surface of the extracted rods along with brittle chipping marks. These streaks also had multiple overlapping sinusoidal lines.

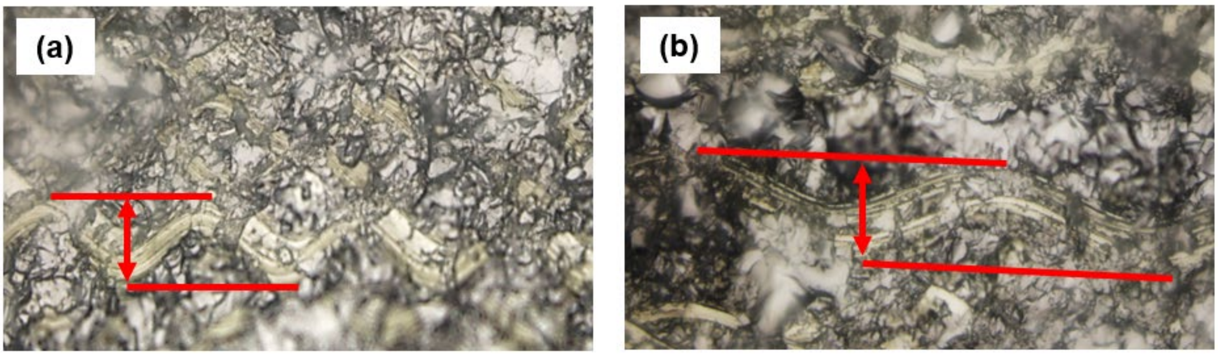

Figure 9. Microscopic images of the rod surfaces. **(a)** Spindle speed: 3500 rpm; **(b)** Spindle speed: 6500 rpm.

The sinusoidal streaks found on the extracted rods indicated that the streaks made with high spindle speed (Figure 9b) had higher wavelength than the streaks made with low spindle speed (Figure 9a), matching with the motion simulation discussed before. Similar streaks and wavelength variation can also be seen during RUM of ductile metals like Titanium [83]. These machining streaks are considered as first indications that material was removed by plastic flow [84]. The reduced cutting force of RUM process also caused lower material removal energy that could influence a more favorable transition of brittle removal to ductile removal [85]. Similar combination of both ductile region and brittle region was reported in machining like precision grinding [86], semi ductile polishing [87], and partial ductile machining of brittle materials [88]. Therefore, there were sufficient evidences to consider the material removal mechanism as a combination of both ductile and brittle material removal in this study.

3.3. Effects of machining parameters

As listed in Table 5, the investigation employed a 2^3 full factorial design to evaluate the effects of feedrate, ultrasonic power, and spindle speed on cutting force and surface roughness. Cutting force and surface roughness results and their experimental conditions are summarized in Table 5.

Table 5. Cutting force and surface roughness data.

Run Order	Feedrate (mm/min)	Ultrasonic power (%)	Spindle speed (rpm)	Surface roughness		Cutting force (N)
				R_a(μm)	R_{max}(μm)	
2	10	40	3500	2.73	15.65	78.21
4	30	40	3500	2.49	15.90	81.57
1	10	60	3500	2.99	18.42	75.32
3	30	60	3500	2.61	14.25	80.44
8	10	40	6500	2.39	15.2	66.11
7	30	40	6500	1.87	11.52	60.39
6	10	60	6500	2.45	13.37	60.59
5	30	60	6500	1.98	12.07	57.56

3.3.1. Cutting force

R Studio was used to study the effects of input parameters on the cutting force. From the initial analysis of variance, a reduced order model having Adjusted R squared value of 0.9833 and 4 degrees of freedom was analyzed. As shown in Table 6, spindle speed had the lowest P- value (0.0003) meaning spindle speed had the most significant effect on cutting force. Secondly, ultrasonic power had a P-value of 0.042, below the significance level of $\alpha = 0.05$, signifying that the cutting force was also strongly influenced by the ultrasonic power. Thirdly, feedrate had a high P-value, indicating that the impact of feedrate within the experimental range employed in this study was insignificant.

Table 6. ANOVA results.

Source	Degrees of freedom	Sum of squares	Mean square	F-Value	P-Value
Model	4	684.42	171.11	104.18	0.002
Feedrate	1	0.01	0.01	0.0055	0.945
Ultrasound	1	19.13	19.13	11.65	0.042
Spindle speed	1	628.17	628.17	382.49	0.0003
Feedrate: Spindle speed	1	37.11	37.11	22.60	0.018
Error	3	4.93	1.64		
Total	7	689.35			

Figure 10a–f depicts the main effects and interaction effects on the cutting force. Figure 10a–c shows that cutting force decreased as spindle speed and ultrasonic power increased while the feedrate effect was insignificant. Furthermore, increasing the spindle speed was more effective in reducing the cutting force than increasing the ultrasonic power. Out of the three two-factor interactions, only the interaction effect between feed rate and spindle speed was significant at a significance level of $\alpha = 0.05$ (Figure 10d–f). It can be seen that both at high and low feedrates, increasing the spindle speed was effective in reducing the cutting force; however, at high feedrate, the effect was more substantial.

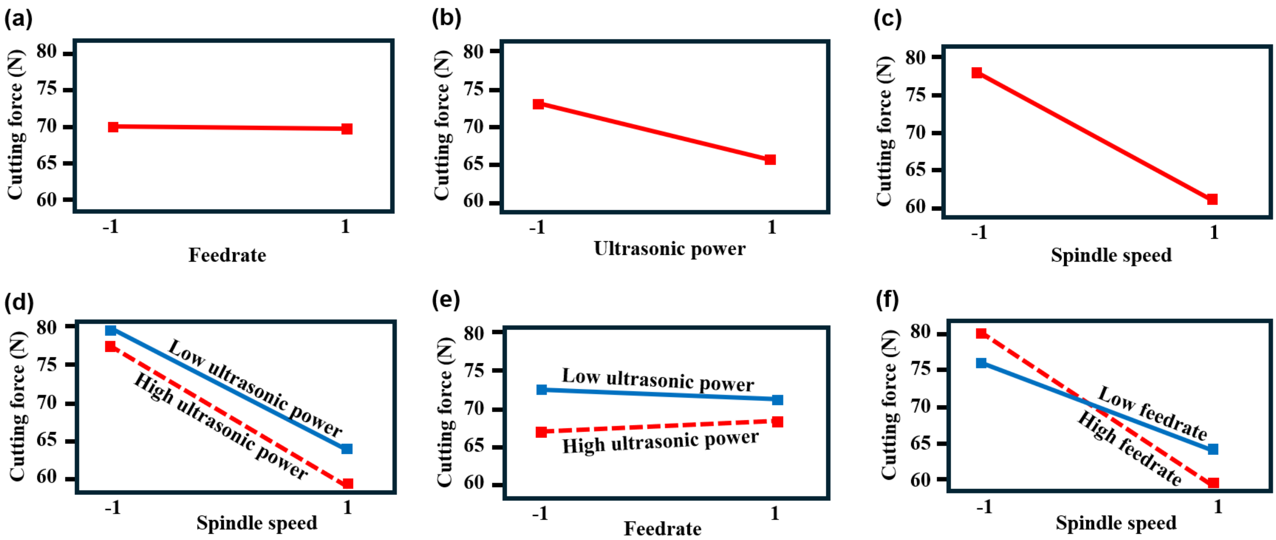

Figure 10. Main effects on cutting force. **(a)** Federate; **(b)** Ultrasonic power; **(c)** Spindle speed, and two factor interactions on cutting force; **(d)** Spindle speed and ultrasonic power; **(e)** Feedrate and ultrasonic power; **(f)** Feedrate and spindle speed.

Four additional experiment conditions were used to extend the range of feedrate to 60 and 120 mm/min. First the ultrasonic power was set to zero with both feedrates and then the ultrasonic power was set to 50% which was lower than the initial design of experiments high level. In all four experiments spindle speed was kept fixed at 5000 rpm. Additional experimental data from higher feedrate is provided in Table 7. It was found that increasing the feedrate by two times without ultrasonic power had a cutting force of 106.33 (N) which was almost 25 (N) more than the measured cutting force with 50% ultrasonic power. When the feedrate was increased by four times without ultrasonic power the cutting force increased significantly. With the introduction of 50% ultrasonic power, cutting force was reduced again signifying the effect of ultrasonic power on reducing the cutting force even at much higher feedrate. Additionally, the surface finish didn't deteriorate, showing RUM's feasibility of machining single-crystal silicon with high feedrate.

Table 7. Experimental results with high federate.

Feedrate (mm/min)	Ultrasonic power (%)	Spindle speed (rpm)	Surface roughness R_a(μm)	Cutting force (N)
60	0	5000	2.54	106.33
60	50	5000	2.47	81.61
120	0	5000	2.2	131.64
120	50	5000	2.19	124.71

To further illustrate the influence of cutting force on material removal behavior, supplementary scratching experiments were conducted. A spindle speed of 1000 rpm was intentionally selected to generate higher cutting forces and accentuate brittle-fracture features, while 6500 rpm was used to represent a low-force condition. Figure 11a,b presents SEM images of imprints on silicon surfaces produced by the RUM cutting tool at spindle speeds of 1000 rpm and 6500 rpm. At the lower spindle speed (1000 rpm), the higher cutting force induced significant brittle fracture and pulverization (Figure 11a). In contrast, at the higher spindle speed (6500 rpm), the reduced cutting force resulted in a surface exhibiting a combination of ductile deformation and brittle fracture, without evidence of pulverization (Figure 11b).

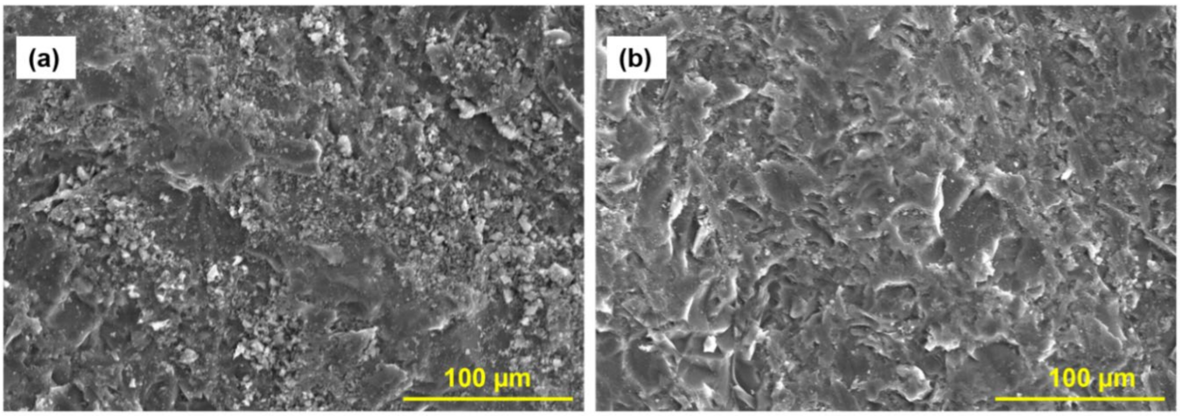

Figure 11. Images of the as machined surface with **(a)** spindle speed 1000 rpm, and **(b)** spindle speed 6500 rpm.

3.3.2. Surface roughness

The measured average roughness (R_a) values for the machined holes were between 2–3 µm for all experiments. The roughness value was comparable to that reported by Smith *et al.* [14], where a CNC vertical milling machine and a high-speed (90,000–100,000 rpm) spindle dressed with miniature diamond cutters were employed to drill monocrystalline silicon block. The holes were 12 mm in diameter and 15 mm in depth. The reported average surface roughness value was 1.14 µm. In case of Electric discharge machining for hole-making in single-crystal silicon, the reported R_{max} values were between 20 µm and 60 µm [21]. The R_{max} values in this study were between 11.52 µm and 18.42 µm as shown in Table 5. The average surface roughness values were between 2.19 µm and 2.54 µm, even when feedrate was increased to 60 mm/min and 120 mm/mm (Table 5). Table 8 summarizes the surface roughness values under conventional machining conditions without ultrasonic vibration assistance. Observed R_a and R_{max} values were spread within similar range of surface roughness values that were machined with ultrasonic vibration assistance. The best surface finish was achieved with ultrasonic power set at 40% and spindle speed set at 6500 rpm, which had an average roughness value of 1.87 µm.

Table 8. Surface roughness values under conventional machining conditions.

Feedrate (mm/min)	Ultrasonic power (%)	Spindle speed (rpm)	Surface roughness	
			R_a(µm)	R_{max}(µm)
10	0	3500	2.72	14.59
10	0	6500	2.57	12.20
30	0	3500	2.16	12.85
30	0	6500	2.09	10.53

3.3.3. Edge chipping

Edge chipping is a challenge associated with RUM of brittle materials as there is a tendency for the rod to break off at the exit of the hole before the tool penetrates the workpiece entirely. Theoretically, edge chipping initiates at a critical cutting depth when the normal maximum stress becomes greater than the ultimate tensile strength [89]. Figure 12 summarizes the chipping size measured across different machining conditions (A–H). Lowering the feedrate reduced chipping in two of four matched comparisons (A *vs.* B, C *vs.* D, E *vs.* F, G *vs.* H). Three out of four comparisons indicated that increasing spindle speed reduced the average chipping size (A *vs.* E, B *vs.* F, C *vs.* G, D *vs.* H). Similarly, increasing ultrasonic power also lowered chipping in three out of the four comparisons (A *vs.* C, B *vs.* D, E *vs.* G, F *vs.* H). On average, ultrasonic power produced the largest reduction in edge chipping (−0.61 mm), followed by spindle speed (−0.24 mm), whereas feedrate exhibited only a marginal influence (−0.08 mm). The smallest edge chipping size was 1.52 mm, achieved under condition G, corresponding to low feedrate, high spindle speed and high ultrasonic power. Edge chipping sizes measured during conventional machining experiments ranged from 1.26 mm to 2.20 mm, which were generally lower than those measured under ultrasonic vibration assistance. Similar behavior has been reported previously and attributed to the intermittent impact loading of diamond abrasives during RUM, where fluctuating abrasive-workpiece interactions can promote localized crack initiation at the hole exit [80]. However, the minimum chipping size of 1.52 mm achieved under condition G demonstrates that appropriate selection of machining parameters can effectively mitigate edge chipping during RUM.

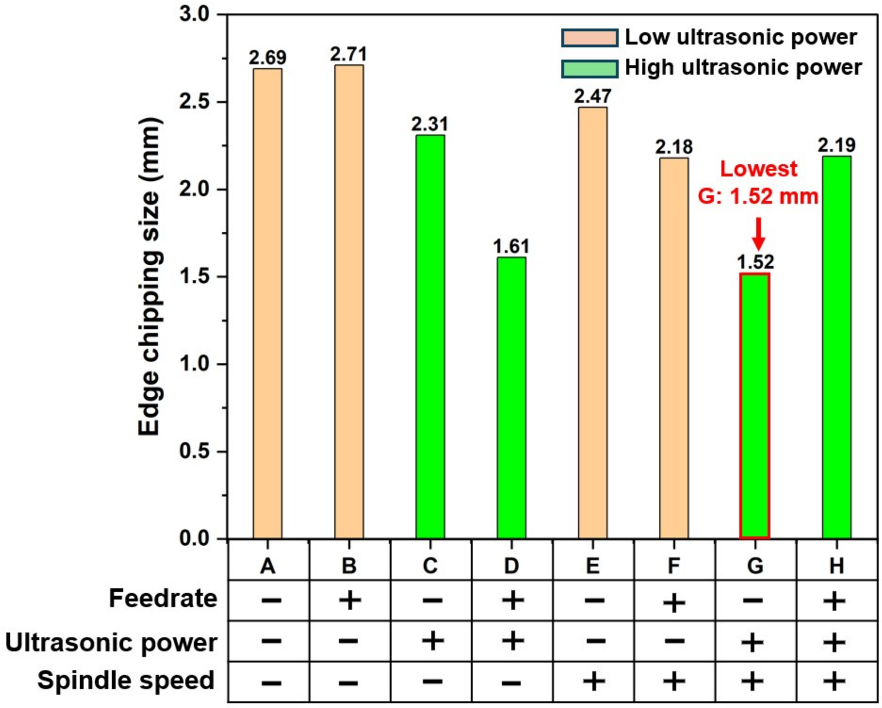

Figure 12. Edge chipping size for different machining conditions (− low, + high).

3.3.4. Geometrical accuracy

To further evaluate the quality of the machined holes, geometrical accuracy was assessed through roundness error, taper angle, and core diameter variability. Figure 13 summarizes the results obtained under different machining conditions. As depicted in Figure 13a the measured roundness errors ranged from 84 to 183 µm. The smallest roundness error was obtained under condition G with low feedrate and increased ultrasonic power and spindle speed. In general, the roundness error was lower with increased spindle speed and ultrasonic power except condition H, where feedrate was also high. The taper angle varied from 0.052° to 0.188° as shown in Figure 13b. The minimum taper angle was achieved under condition G, indicating the formation of nearly cylindrical hole. Similar to the roundness results, increasing spindle speed and ultrasonic power generally reduced the taper angle, suggesting improved dimensional consistency along the hole depth. Figure 13c presents the standard deviation of the extracted core diameter, which was used to characterize diameter variability and dimensional consistency. Similar to roundness error and taper angle, the diameter variability was improved with increased ultrasonic power and spindle speed.

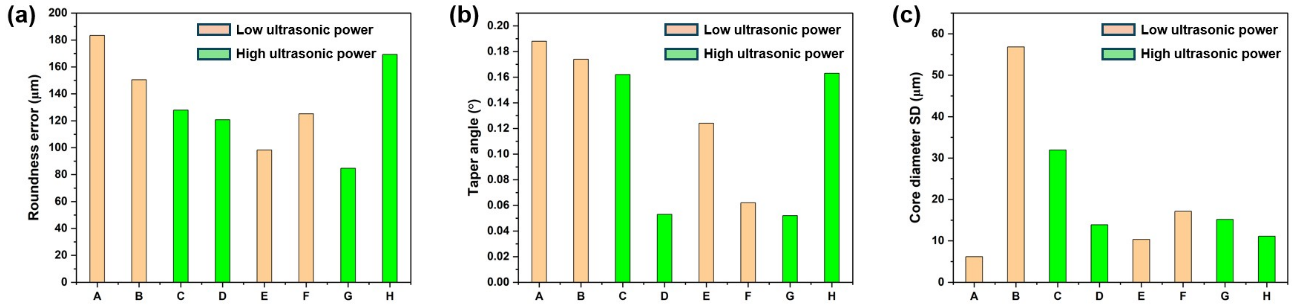

Figure 13. Geometrical accuracy under different machining conditions. **(a)** Hole-exit roundness error; **(b)** Taper angle; **(c)** Standard deviation of core diameter.

Additional experiments were conducted to further investigate the influence of ultrasonic vibration assistance on geometrical accuracy. The results are summarized in Table 9. Without ultrasonic vibration assistance, the range for both taper angle and diameter variability was increased except for the roundness error. In addition, increasing feedrate under conventional machining condition resulted in larger roundness errors and greater core diameter variability. These results indicate that the combination of high spindle speed, high ultrasonic power, and low feedrate is favorable for improving the geometrical accuracy of holes machined in single-crystal silicon.

Table 9. Geometrical accuracy under conventional machining conditions.

Feedrate (mm/min)	Ultrasonic power (%)	Spindle speed (rpm)	Roundness error (µm)	Taper angle (°)	Standard deviation (µm)
10	0	3500	105.68	0.275	20.23
10	0	6500	107.69	0.374	11.95
30	0	3500	137.36	0.084	89.38
30	0	6500	123.10	0.106	67.55

3.4. Tool wear

Tool wear during RUM of single-crystal silicon was assessed by comparing optical micrographs of the cutting edge captured before and after completing the hole drilling sequence. It was observed that nearly all the diamond abrasives remained intact at the same locations across the two images with little visible degradation. Further in-depth wear mechanism study distinguished three wear modes: attritious wear (Figure 14a), grain fracture (Figure 14b), and bond fracture (Figure 14 c). Attritious wear is characterized by progressive blunting and polishing of the abrasive surfaces from sustained frictional sliding against the workpiece. Attritious wear was identified as the prevalent wear mode whereas signatures of grain fracture and bond fracture were scarce. Grain fracture typically arises under intense impact or thermomechanical loading causing localized chipping and shattering of individual diamond abrasive. On the other hand, bond fracture is characterized by failure of the metallic bond matrix and dislodging of the abrasives from tool surface. The limited occurrence of these two wear modes could be explained by the reduced cutting stress from the intermittent cutting action of RUM.

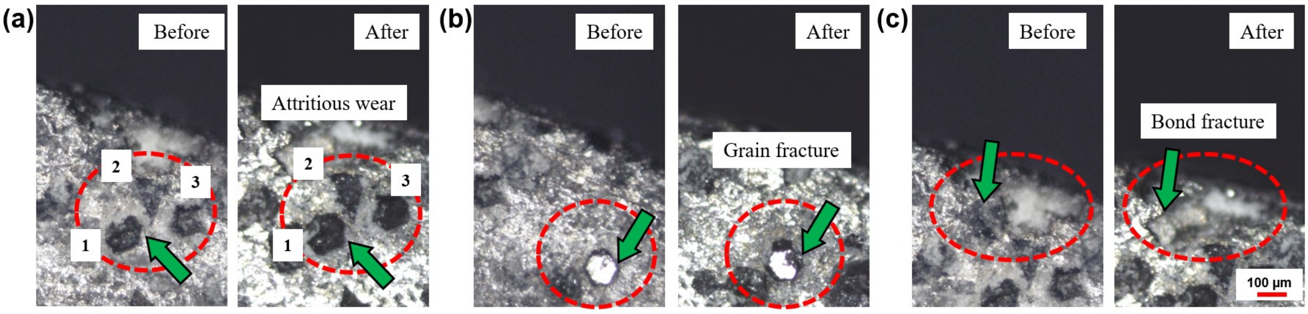

Figure 14. Wear modes observed on the cutting tool after machining with ultrasonic vibration assistance. **(a)** Attritious wear (blunting and polishing of abrasives); **(b)** Grain fracture (corner chipping of diamond abrasive); **(c)** Bond fracture (failure of the metallic bond).

For comparison, similar tool wear observations were performed after conventional machining without ultrasonic vibration assistance. The tool surface after conventional machining experiments exhibited a greater number of bond-fracture signatures and more pronounced longitudinal grooves (Figure 15a,b). These observations suggest that cutting stress was higher during conventional machining, which promoted more severe abrasive and bond degradation. In contrast, the reduction in cutting force achieved through ultrasonic vibration assistance mitigated mechanical loading on both diamond abrasives and bond material, thereby suppressing catastrophic wear modes.

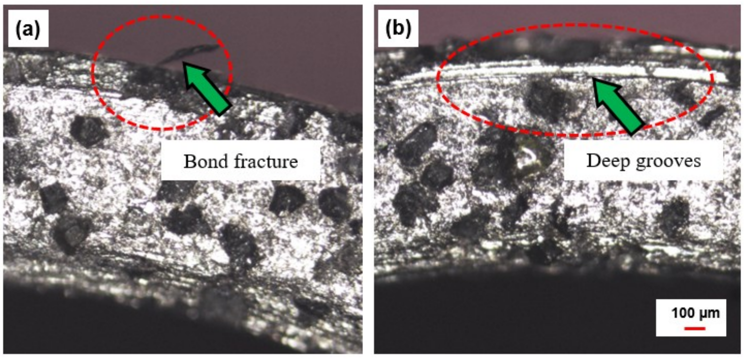

Figure 15. Tool wear signatures after conventional machining. **(a)** Bond fracture; **(b)** Long deep grooves.

4. Conclusion

This investigation provides a comprehensive analysis on RUM for hole-making operations in single-crystal silicon, demonstrating both technical feasibility and revealing insights into its material removal mechanism. The effects of machining parameters (spindle speed, ultrasonic power, and feedrate) on the cutting force, hole surface quality and geometrical accuracy were evaluated, along with edge chipping size and cutting tool wear analysis. The following conclusions can be drawn:

- The material removal mechanism during RUM of single-crystal silicon was identified as a hybrid ductile-brittle mode. Nanoindentation experiments with superimposed oscillation showed enhanced plastic deformation without generating radial cracks, whereas microscopy observations revealed the coexistence of material pile-up, sinusoidal machining streaks and brittle fracture. Localized crack suppression, pressure-induced phase transformation and reduced penetration depth likely contributed to promoting ductile deformation during RUM, while brittle fracture remained an active material removal mechanism.

- Ultrasonic vibration assistance reduced cutting forces by up to 29%, and extended feedrate tests demonstrated that the force-reduction effect persisted even under substantially increased feedrates. At the same time, the surface roughness, geometrical accuracy of the holes, and edge chipping sizes at the hole exit were comparable to or better controlled than those obtained under conventional machining conditions. The combination of low feedrate, high spindle speed, and high ultrasonic power produced the best overall surface quality and geometrical accuracy.
- Minimal tool wear was observed as the diamond abrasives remained largely intact throughout all experiments. Attritious wear was identified as the dominant wear mechanism during RUM and compared with conventional machining conditions, ultrasonic vibration assistance reduced severe wear signatures by lowering the mechanical loading on both diamond abrasives and bond material.

Supplementary data

Calculation for the maximum pressure during RUM is provided with this article. Table S1 summarizes the calculated pressure values corresponding to abrasive size and cutting force.

Data availability statement

The datasets generated and analyzed in this study are available in Zenodo repository at https://doi.org/10.5281/zenodo.22085124.

Declaration of generative AI and AI-assisted technologies

During the preparation of this manuscript, the authors used generative AI tools only to improve language and readability. Specifically, the authors used Microsoft copilot for language polishing and proofreading. The authors take full responsibility for the content of the manuscript.

Acknowledgments

Funding: The authors declare that no funds, grants, or other support were received during the preparation of this manuscript. The authors acknowledge the Materials Characterization Laboratory (MCL), the Office of the Vice President for Research (OVPR), and the College of Engineering at Kansas State University for providing access to characterization facilities used in this study.

Authors' contribution

Conceptualization, all authors; methodology, K.M.A.R.; investigation, K.M.A.R., I.O. and D.W.; formal analysis and visualization, K.M.A.R.; writing—original draft, K.M.A.R.; writing—review and editing, M.Z. and C.J.; supervision, M.Z. All authors have read and agreed to the published version of the manuscript.

Conflicts of interest

Deven Wieland is an employee of John Deere. The author declares that this affiliation does not influence the design, analysis, interpretation, or presentation of the results reported in this manuscript. The authors declare no other conflicts of interest associated with this manuscript.

References

[1] Vasanthi N, Saleena LM, Raj SA. Silicon in day today life. *World Appl. Sci. J.* 2012, 17(11):1425–1440.

[2] Angell JB, Terry SC, Barth PW. Silicon micromechanical devices. *Sci. Am*. 1983, 248(4):44–55.

[3] Tilli M, Haapalinna A. Properties of silicon. In *Handbook of Silicon Based MEMS Materials and Technologies*, 3rd ed. Amsterdam: Elsevier, 2020. pp. 3–17.

[4] Ehrlich HL, Newman DK, Kappler A. *Ehrlich's Geomicrobiology*, 6th ed. Boca Raton: CRC Press, 2015.

[5] Abe N. Method and apparatus for dry etching and electrostatic chucking device used therein. US patent US4384918A, 1983. Available: https://patents.google.com/patent/US4384918A/en (accessed on 13 January 2025).

[6] Noorbakhsh H, Carducci JD, Sun JY, Elizaga LD. Gas distribution showerhead for semiconductor processing. US patent US6983892B2, 2006. Available: https://patents.google.com/patent/US6983892B2/en (accessed on 23 April 2025).

[7] Ouyang Z, Ruzic DN, Kiehlbauch M, Schrinsky A, Torek K. Etching mechanism of the single-step through-silicon-via dry etch using SF6/C4F8 chemistry. *J. Vac. Sci. Technol. A* 2014, 32(4):041306.

[8] Li A, Hu S, Zhou Y, Wang H, Zhang Z, *et al*. Recent advances in precision diamond wire sawing monocrystalline silicon. *Micromachines* 2023,14(8):1512.

[9] Leung TP, Lee WB, Lu X. Diamond turning of silicon substrates in ductile-regime. *J. Mater. Process. Technol*. 1998, 73(1):42–48.

[10] Zhou M, Ngoi BKA, Zhong ZW, Chin CS. Brittle-ductile transition in diamond cutting of silicon single crystals. *Mater. Manuf. Process*. 2001, 16(4):447–460.

[11] Ebrahimi F, Kalwani L. Fracture anisotropy in silicon single crystal. *Mater. Sci. Eng. A* 1999, 268(1):116–126.

[12] Debnath S, Kunar S, Anasane SS, Bhattacharyya B. Non-traditional micromachining processes: opportunities and challenges. In *Non-Traditional Micromachining Processes: Fundamentals and Applications*. Cham: Springer International Publishing, 2017. pp. 1–59.

[13] Daud ND, Hasan MdN, Saleh T, Leow PL, Mohamed Ali MS. Non-traditional machining techniques for silicon wafers. *Int. J. Adv. Manuf. Technol*. 2022, 121(1):29–57.

[14] Smith ST. Machining of silicon using high-speed miniature diamond cutters. *J. Phys. Appl. Phys*. 1990, 23(5):607.

[15] Luft A, Franz U, Emsermann L, Kaspar J. A study of thermal and mechanical effects on materials induced by pulsed laser drilling. *Appl. Phys. A* 1996, 63(2):93–101.

[16] Lee YH, Choi KJ. Analysis of silicon via hole drilling for wafer level chip stacking by UV laser. *Int. J. Precis. Eng. Manuf.* 2010, 11(4):501–507.

[17] Tang CW, Li KM, Yang M, Liao HC, Young HT. Improving the dielectric breakdown field of silicon light-emitting-diode sub-mount by a hybrid nanosecond laser drilling strategy. *Microelectron. Reliab*. 2013, 53(3):420–427.

[18] Wang HJ, Yang T. A review on laser drilling and cutting of silicon. *J. Eur. Ceram. Soc*. 2021, 41(10):4997–5015.
[19] Ostendorf A, Kamlage G, Klug U, Korte F, Chichkov BN. Femtosecond versus picosecond laser ablation. In *Proceedings of Photon Processing in Microelectronics and Photonics IV*, San Jose, USA, January 24–27, 2005, pp. 1–8.
[20] Maclean JO, Tangkijcharoenchai C, Coomber S, Voisey KT. Laser drilling of micro-holes in single crystal silicon, indium phosphide and indium antimonide using a continuous wave (CW) 1070 nm fibre laser with millisecond pulse widths. *Procedia CIRP* 2018, 74:407–412.
[21] Unoa Y, Okada A, Okamoto Y, Yamazaki K, Risbud SH, *et al*. High efficiency fine boring of monocrystalline silicon ingot by electrical discharge machining. *Precis. Eng*. 1999, 23(2):126–133.
[22] Mohammadi H, Patten JA. Laser augmented diamond drilling: a new technique to drill hard and brittle materials. *Procedia Manuf*. 2016, 5:1337–1347.
[23] Kumar S, Dvivedi A. Micro-ultrasonic drilling of monocrystalline silicon: an experimental investigation on machined surface topography and optimization using User's preference rating based TOPSIS. *Mater. Sci. Semicond. Process*. 2019, 102:104584.
[24] Martins H, Puga H. Ultrasonic assisted machining overview: accessing feasibility and overcoming challenges for milling applications. *Metals* 2023, 13(5):908.
[25] Singh J, Singh C, Singh K. Rotary ultrasonic machining of advance materials: a review. *Mater. Today Proc.* 2026, 116:81–86.
[26] Pandey H, Apurva A, Dixit P. Investigations into velocity decay, initial tool-workpiece gap, and material removal behaviour in ultrasonic micromachining. *J. Manuf. Process*. 2024, 124:52–67.
[27] Du B, Wang J, Yuan J, Lyu B, Zhang X, *et al*. Material removal characteristics of spherical-array-focused ultrasonic abrasive machining. *Micromachines* 2023, 14(2):382.
[28] Banerjee B, Pradhan S, Das S, Dhupal D. Surface topography characterization of USMM during machining of zirconia ceramic using silicon carbide abrasives: an experimental and simulation approach. *CIRP J. Manuf. Sci. Technol*. 2024, 51:1–19.
[29] Zhao J, Xu X, Li W, Hang W. Material removal modes and processing mechanism in microultrasonic machining of ball ceramic tool. *Ceram. Int*. 2024, 50(16):28844–28856.
[30] Li S, Wen S, Qiao J, Feng M. Experimental study on hydrogen embrittlement-enhanced ultrasonic machining of inconel 718 small hole. *Appl. Sci*. 2024, 14(20):9319.
[31] Mirad MM, Das B. Machine learning coupled with acoustic emission signal features for tool wear estimation during ultrasonic machining of Inconel 718. *Mach. Sci. Technol*. 2024, 28(2):119–142.
[32] Wang H, Zhang H, Zhou M. Study on surface defect formation mechanism in ultrasonic vibration-assisted grinding of SiCp/Al composites. *Int. J. Adv. Manuf. Technol*. 2023, 129(1):375–397.
[33] Zhou Y, Jia S, Lu Y, Liu J, Ma L, *et al*. Study on ultrasonic elliptical vibration-assisted grinding mechanism and surface quality of C/SiC composite material. *Diam. Relat. Mater*. 2024, 149:111565.
[34] Lv D, Chen G, Liu D, Xu H, Chen M, *et al*. High-frequency vibration effects on material removal mechanisms in ultrasonic transverse scratching of carbon fiber reinforced plastics. *Ultrasonics* 2023, 132:106979.
[35] Sun Q, Ren K, An Q, Tao D, Yu M, *et al*. Study on removal mechanism and surface quality of SiCf/SiC composites by longitudinal torsional ultrasonic vibration-assisted grinding. *Precis. Eng*. 2024, 91:47–58.

[36] Dong Z, Yuan G, Ran Y, Sun H, Sun J, *et al*. Material removal mechanism of SiCf/SiC composites during ultrasonic-assisted scratching with vertical vibration. *Chin. J. Aeronaut*. 2025, 103416.

[37] Ding K, Li Q, Zhang C. Experimental studies on material removal mechanisms in ultrasonic assisted grinding of SiC ceramics with a defined grain distribution brazed grinding wheel. *Int. J. Adv. Manuf. Technol*. 2021, 116(11):3663–3676.

[38] Qiao G, Yi S, Zheng W, Zhou M. Material removal behavior and crack-inhibiting effect in ultrasonic vibration-assisted scratching of silicon nitride ceramics. *Ceram. Int*. 2022, 48(3):4341–4351.

[39] Zhao M, Xue B, Li B, Zhu J, WenbinSong, *et al*. Modeling of grinding force in longitudinal ultrasonic vibration–assisted grinding alumina ceramics and experimental evaluation. *Int. J. Adv. Manuf. Technol*. 2024, 131(5):2325–2339.

[40] Ma Z, Meng F, Cui Z, Chen L, Zhang C, *et al*. Surface formation mechanism in ultrasonic vibration assisted grinding dental zirconia ceramic process considering stochasticity of grits. *J. Mater. Res. Technol*. 2025, 36:2718–2730.

[41] Cao Y, Ding W, Zhao B, Wen X, Li S, *et al*. Effect of intermittent cutting behavior on the ultrasonic vibration-assisted grinding performance of Inconel718 nickel-based superalloy. *Precis. Eng*. 2022, 78:248–260.

[42] You H, Zhao B, Ding W, Miao Q, Yang C, *et al*. Wear behavior of white alumina and seeded gel abrasive wheels in ultrasonic vibration-assisted grinding of nickel-based single-crystal alloy. *Wear*. 2024, 556–557:205505.

[43] Chen T, Wang X, Zhao B, Ding W, Xiong M, *et al*. Material removal mechanisms in ultrasonic vibration-assisted high-efficiency deep grinding γ-TiAl alloy. *Chin. J. Aeronaut*. 2024, 37(11):462–476.

[44] Li P, Xu J, Zuo H, Wang H, Liu Y. The material removal mechanism and surface characteristics of Ti-6Al-4 V alloy processed by longitudinal-torsional ultrasonic-assisted grinding. *Int. J. Adv. Manuf. Technol*. 2022, 119(11):7889–7902.

[45] Zhang D, Li H, Tang J, Huang W. Cutting mechanism and surface characteristics of during ultrasonic vibration-assisted cutting iron alloy: an atomistic investigation. *Tribol. Int*. 2026, 214:111275.

[46] Sun G, Zhang W, Wang J, Ding J, Wang B, *et al*. Research on subsurface damage mechanism and suppression method of ultrasonic vibration–assisted grinding of sapphire components under extreme service environment. *Int. J. Adv. Manuf. Technol*. 2024, 135(5):2215–2242.

[47] Chen Y, Hu Z, Yu Y, Lai Z, Zhu J, *et al*. Processing and machining mechanism of ultrasonic vibration-assisted grinding on sapphire. *Mater. Sci. Semicond. Process*. 2022, 142:106470.

[48] Liu X, Yi J, Wang T, Zheng Z, Gong T, *et al*. Longitudinal torsional ultrasonic vibratory assistant milling of borosilicate glass material removal mechanism based on the thickness of undeformed chips. *Ceram. Int*. 2024, 50(24):53230–53244.

[49] Zhang W, Cui E, Zhang B, Wang M, Zhao X. Study on the material removal mechanism and the exit breakage of ultrasonic vibration-assisted grinding for microcrystalline glass. *Discover Appl. Sci*. 2024, 6(3):133.

[50] Ming W, Cai C, Ma Z, Nie P, Li C, *et al*. Milling mechanism and surface roughness prediction model in ultrasonic vibration-assisted side milling of Ti–6Al–4 V. *Int. J. Adv. Manuf. Technol*. 2024, 131(5):2279–2293.

[51] Wang X, He Q, Zhao B, Ding W, Su H, *et al*. Material removal and surface texture in the longitudinal ultrasonic vibration-assisted milling of GH4169D superalloy. *Front. Mech. Eng*. 2025, 20(2):13.

[52] Khan A, He Q, Wang X, Zhao B, Ding W, *et al*. Unraveling the influence of vibrations on material removal and surface quality in longitudinal ultrasonic vibration–assisted milling of Ti2AlNb intermetallic alloy. *Int. J. Adv. Manuf. Technol*. 2025, 136(5):2507–2525.

[53] Xie W, Wang X, Zhao B, Li G, Xie Z. Surface and subsurface analysis of TC18 titanium alloy subject to longitudinal-torsional ultrasonic vibration-assisted end milling. *J. Alloys. Compd*. 2022, 929:167259.

[54] Jing L, Niu Q, Yue W, Rong J, Gao H, Tang S. Groove bottom material removal mechanism and machinability evaluation for longitudinal ultrasonic vibration–assisted milling of Al-50 wt % Si alloy. *Int. J. Adv. Manuf. Technol*. 2023, 127(1):365–380.

[55] Shi Z, Xiang D, Feng H, Wu B, Zhang Z, *et al*. Finite element and experimental analysis of ultrasonic vibration milling of high-volume fraction SiCp/Al composites. *Int. J. Precis. Eng. Manuf*. 2021, 22(10):1777–1789.

[56] Chen G, Xu J, Wang J, Li Y, Wang J, *et al*. Numerical and experimental study on the amplitude effect of ultrasonic vibration-assisted milling of 3D needle-punched Cf/SiC composite. *Ceram. Int*. 2022, 48(12):17893–17914.

[57] Xie Z, Liu Z, Wang B, Xin M, Song Q, *et al*. Longitudinal amplitude effect on material removal mechanism of ultrasonic vibration-assisted milling 2.5D C/SiC composites. *Ceram. Int*. 2021, 47(22):32144–32152.

[58] Liu W, Shan C, Wang S, Jia F, Xia Z. Ultrasonic vibration assisted milling of C/C composites: Mechanism, machining characteristics, and parameters optimization. *Compos. Part B Eng*. 2026, 316:113555.

[59] Lu M, Guo K, Du Y, Lin J, Jia H. Modeling of cutting forces and removal mechanisms of silicon carbide fiber-reinforced aluminum matrix composites under ultrasonic elliptical vibration cutting. *J. Manuf. Process*. 2026, 167:1–16.

[60] Liang Y, Zhang C, Chen X, Zhang T, Yu T, *et al*. Modeling and analysis of the material removal rate for ultrasonic vibration–assisted polishing of optical glass BK7. *Int. J. Adv. Manuf. Technol*. 2022, 118(1):627–639.

[61] Cui Z, Liang Y, Chen X, Meng F, Wang Z, *et al*. The ultrasonic vibration–assisted polishing material removal model of tilted cylindrical polishing tool based on BK7 glass. *Int. J. Adv. Manuf. Technol*. 2023, 125(5):2797–2814.

[62] Huang Z, Shi C, Li G, Zou Z, Zhang S, *et al*. Material removal mechanisms in self-excited vibration polishing of optical surfaces using an eccentric flexible ball-end tool. *Precis. Eng*. 2026, 102:526–552.

[63] Liu D, Li J, Xian C, Gu Z. Study on material removal by ultrasonic vibration-assisted polishing of silicon carbide wafer (4H-SiC). *Mater. Sci. Semicond. Process*. 2026, 204:110318.

[64] Chen F, Bie W, Wang X, Zhao B. Longitudinal-torsional coupled rotary ultrasonic machining of ZrO2 ceramics: an experimental study. *Ceram. Int*. 2022, 48(19):28154–28162.

[65] Chen F, Bie W, Chang Y, Zhao B, Wang X, *et al*. Analytical and experimental investigation on cutting force in longitudinal-torsional coupled rotary ultrasonic machining zirconia ceramics. *Int. J. Adv. Manuf. Technol*. 2022, 120(5):4051–4064.

[66] Sun G, Wang S, Zhao Q, Ji X, Ding J. Material removal and surface generation mechanisms in rotary ultrasonic vibration–assisted aspheric grinding of glass ceramics. *Int. J. Adv. Manuf. Technol*. 2024, 130(7):3721–3740.

[67] Zhang Z, Jiao F, Li Y, Wang X, Niu Y, *et al*. Experimental study on rotary longitudinal-torsional ultrasonic machining of unidirectional CFRP. *Chin. J. Aeronaut*. 2024, 37(11):517–534.
[68] Jin J, Wang X, Bie W, Chen F, Zhao B. Machinability of SiCf/SiC ceramic matrix composites using longitudinal-torsional coupled rotary ultrasonic machining. *Int. J. Adv. Manuf. Technol*. 2024, 131(5):2465–2476.
[69] Yao L, Liu Z, Song Q, Wang B, Cai Y, *et al*. Debonding fiber damage mechanism modeling for machining damage inhibition during rotary ultrasonic face grinding SiO2f/SiO2. *J. Manuf. Sci. Eng*. 2024, 146(11):111003.
[70] Cao S, Zhang X, Wu C, Yang M, Xia K. Towards understanding the material removal mechanism on the effect of ultrasonic vibration and anisotropy for unidirectional CFRP by scratching. *J. Mater. Process. Technol*. 2024, 324:118250.
[71] Lawn B. *Fracture of Brittle Solids*, 2nd ed. Cambridge: Cambridge University Press, 1993.
[72] Luo J, Vargheese KD, Tandia A, Hu G, Mauro JC. Crack nucleation criterion and its application to impact indentation in glasses. *Sci. Rep*. 2016, 6(1):23720.
[73] Marshall DB, Lawn BR, Evans AG. Elastic/plastic indentation damage in ceramics: the lateral crack system. *J. Am. Ceram. Soc*. 1982, 65(11):561–566.
[74] Griffith AA. The phenomena of rupture and flow in solids. *Philos. Trans. R. Soc. Lond. A Math. Phys. Eng. Sci.* 1921, 221:163–198.
[75] Anderson TL. *Fracture Mechanics: Fundamentals and Applications*, 3rd ed. Boca Raton: CRC Press, 2005.
[76] Crain J. Reversible pressure-induced structural transitions between metastable phases of silicon. *Phys. Rev. B* 1994, 50(17):13043–13046.
[77] Hu JZ. Crystal data for high-pressure phases of silicon. *Phys. Rev. B* 1986, 34(7):4679–4684.
[78] Bifano TG, Dow TA, Scattergood RO. Ductile-regime grinding: a new technology for machining brittle materials. *J. Eng. Ind*. 1991, 113(2):184–189.
[79] O'Connor BP, Marsh ER, Couey JA. On the effect of crystallographic orientation on ductile material removal in silicon. *Precis. Eng*. 2005, 29(1):124–132.
[80] Li Y, Zhang D, Wang H, Ye G, He R, *et al*. Theoretical and experimental investigations on rotary ultrasonic surface micro-machining of brittle materials. *Ultrason. Sonochem*. 2022, 89:106162.
[81] Fernando PKSC, Pei ZJ, Zhang M. Mechanistic cutting force model for rotary ultrasonic machining of rocks. *Int. J. Adv. Manuf. Technol*. 2020, 109(1):109–128.
[82] Lockett FJ. Indentation of a rigid/plastic material by a conical indenter. *J. Mech. Phys. Solids*. 1963, 11(5):345–355.
[83] Cong WL, Pei ZJ, Mohanty N, Van Vleet E, Treadwell C. Vibration amplitude in rotary ultrasonic machining: a novel measurement method and effects of process variables. *J. Manuf. Sci. Eng*. 2011, 133:034501.
[84] Santos MVR dos, Damião AJ, Abdalla AJ. High-quality finishing process for silicon carbide optical components using conventional equipment. *Mater. Res*. 2022, 25:e20210422.
[85] Neo WK, Kumar AS, Rahman M. A review on the current research trends in ductile regime machining. *Int. J. Adv. Manuf. Technol*. 2012, 63(5):465–480.
[86] Venkatesh VC, Izman S, Sharif S, Mon TT, Konneh M. Ductile streaks in precision grinding of hard and brittle materials. *Sadhana* 2003, 28(5):915–924.

[87] Zhong Z, Venkatesh VC. Semi-ductile grinding and polishing of ophthalmic aspherics and spherics*. *CIRP Ann. Manuf. Technol.* 1995, 44(1):339–342.
[88] Zhong ZW. Ductile or partial ductile mode machining of brittle materials. *Int. J. Adv. Manuf. Technol*. 2003, 21(8):579–585.
[89] Beer F, Johnston E, DeWolf J, Mazurek D. Transformations of stress and strain. In *Mechanics of Materials*, 8th ed. New York: McGraw Hill, 2020.